

# Simulation of feedback instability in the coupled magnetosphere-ionosphere system

journal or publication title	Jouenal of Geophysical Research Space Physics
volume	115
page range	A08304
year	2010-08-04
URL	<a href="http://hdl.handle.net/10655/00012514">http://hdl.handle.net/10655/00012514</a>

doi: <https://doi.org/10.1029/2009JA015093>



# Simulation of feedback instability in the coupled magnetosphere-ionosphere system

Hiroki Hasegawa,<sup>1,2</sup> Nobuaki Ohno,<sup>3</sup> and Tetsuya Sato<sup>4</sup>

Received 18 November 2009; revised 9 April 2010; accepted 16 April 2010; published 4 August 2010.

[1] Quiet auroral arcs formation has been investigated theoretically and numerically in a self-consistent dynamic way. By using a three-dimensional magneto-hydro-dynamics simulation of a dipole magnetosphere-ionosphere coupling system, it is shown that multiple longitudinally striated structures of the ionospheric plasma density and the field-aligned current are formed, resulting from nonlinear feedback instability. The areas where these structures appear are consistent with the prediction by the integrated feedback theory that includes the effects of the spatially non-uniform electric field and non-uniform plasma density. Effects of the difference of the field line lengths between the ionosphere and the magnetospheric equator over the auroral latitudes are also discussed on the feedback instability.

**Citation:** Hasegawa, H., N. Ohno, and T. Sato (2010), Simulation of feedback instability in the coupled magnetosphere-ionosphere system, *J. Geophys. Res.*, 115, A08304, doi:10.1029/2009JA015093.

## 1. Introduction

[2] Formation of quiet auroral arcs was investigated theoretically based on different models of the magnetosphere-ionosphere (M-I) coupling system by many authors [Atkinson, 1970; Ogawa and Sato, 1971; Sato and Holzer, 1973; Holzer and Sato, 1973] in 1970s. Then, Sato [1978] integrated these studies and concluded that a quiet auroral arc is formed by a feedback instability that arises spontaneously between the inductive magnetosphere and the dissipative ionosphere. In the vicinity of the magnetospheric equator, the plasma convection flow can be generated by the solar wind as shown in Figure 1. The region 1 current system between the magnetosphere and the ionosphere [Iijima and Potemra, 1976; Sato and Iijima, 1979] is expected to be formed by the electric charges (electric potential) which are induced by the magnetospheric plasma convection flow. In such a global convection-current system, a feedback instability can be produced as a result of the resonance of the ionospheric electrostatic wave with the magnetospheric Alfvén wave.

[3] Further, the ionospheric feedback instability has been studied by many authors. While Sato [1978] assumed that the ionospheric dynamics is described by the height-integrated ionospheric equations and ignored the curvature of the magnetospheric field line, Trakhtengertz and Feldstein

[1984] considered the actual height profile of charge particles velocity in the ionosphere and the curvature of the field line. Also, Lysak [1986, 1988, 1991] showed that the gradient in the Alfvén speed profile has an influence on the propagation of the Alfvén waves and that a locally resonant feedback instability is produced by the inhomogeneity of the Alfvén speed, which was not considered by Sato [1978].

[4] So far, a number of two-dimensional magneto-hydro-dynamics (MHD) simulations for the ionospheric feedback instability have been carried out [Lysak and Song, 2002; Pokhotelov et al., 2002a, 2002b; Streltsov and Lotko, 2003, 2004; Lu et al., 2008]. Some results of these simulations are in good agreement with observational studies about a seasonal variation of discrete aurorae and a relation between solar activity and aurorae [Newell et al., 1996, 1998]. Also, other ionospheric phenomena which are expected to be described by the feedback instability were observed [Nilsson et al., 2005; Chaston et al., 2006; Kozlovsky et al., 2007].

[5] However, in such two-dimensional simulations, the longitudinal dynamics and the effect of the Hall conductivity are ignored. On the other hand, three-dimensional MHD simulations on the basis of the feedback theory include them and have been carried out in order to demonstrate the formation of quiet auroral arcs [Watanabe et al., 1986; Watanabe and Sato, 1988; Watanabe et al., 1993]. Watanabe et al. [1986] developed a three-dimensional MHD code that adopted a radially extending monopole field system and showed generation of a region 1 current system for a twin-vortex convection flow in the magnetospheric equatorial plane and then the appearance of Heppner's ionospheric electric field pattern over the polar cap region [Heppner, 1977]. In the work of Watanabe and Sato [1988], by using the same code, it is shown that longitudinally striated structures of the field-aligned current and the ionospheric plasma density were generated by the feedback instability.

<sup>1</sup>Institute for Research on Earth Evolution, Japan Agency for Marine-Earth Science and Technology, Yokohama, Japan.

<sup>2</sup>Now at Department of Helical Plasma Research, National Institute for Fusion Science, Toki, Japan.

<sup>3</sup>Earth Simulator Center, Japan Agency for Marine-Earth Science and Technology, Yokohama, Japan.

<sup>4</sup>University of Hyogo, Kobe, Japan.

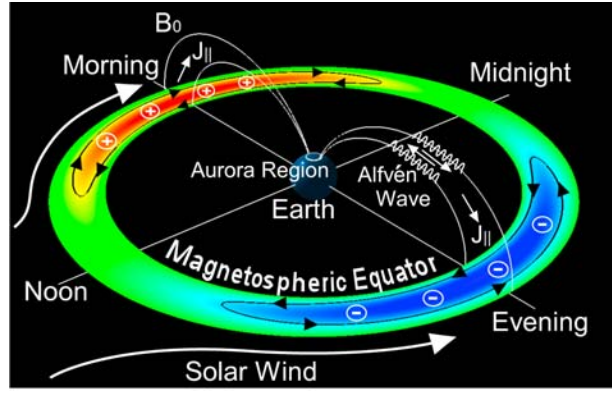


**Figure 1.** Schematic diagram showing geometry of the coupled magnetosphere-ionosphere system.

[6] In those studies, however, the curvature of the magnetospheric field line was neglected. Further, the length of the field line from the ionosphere to the magnetospheric equator was assumed to be uniform everywhere. Most significantly, the generation of high energy auroral electrons along the field lines is treated as a very simple parameterized model without solving the particle acceleration microscopic process.

[7] In a recent paper [Sato *et al.*, 2009], a self-consistent holistic simulation has been successfully carried out based on the Macro-Micro Interlocked (MMI) algorithm [Sato, 2005]. A three-dimensional dipole geomagnetic field represented on the dipole coordinates [Kageyama *et al.*, 2006] was adopted in the numerical model.

[8] This paper describes the integrated theory of the feedback instability and presents detailed results and the robustness of the MHD (macroscopic) simulation (without microscopic processes) from Sato *et al.* [2009]. In section 2, we review the theory of the feedback instability. The effects of the non-uniform ionospheric electric field, the non-uniform ionospheric plasma density, and the non-uniform field line length on the instability are discussed. In section 3, after describing the numerical model of the three-dimensional dipole M-I coupling system, we present the results and the implications of the simulation runs. It is interesting to note that longitudinally striated structures have beautifully grown. The distribution of these structures is in good agreement with that of the theoretically predicted growth rate. We then examine the dependence of the instability on the Pedersen mobility, i.e., the ionospheric density. In section 4, we summarize our work.

## 2. Feedback Instability

### 2.1. Theory of Feedback Instability

[9] First, we briefly review Sato's feedback instability theory [Sato, 1978].

[10] The continuity equation of the ionospheric plasma density is given as

$$\frac{\partial n}{\partial t} + \frac{\mathbf{E}_\perp \times \mathbf{B}_0}{|\mathbf{B}_0|^2} \cdot \nabla_\perp n = \frac{j_\parallel}{eh} - \alpha(n^2 - n_0^2). \quad (1)$$

[11] The current continuity equation is

$$\nabla_\perp \cdot \mathbf{I}_\perp = -j_\parallel. \quad (2)$$

[12] The height-integrated ionospheric current  $\mathbf{I}_\perp$  is given by

$$\mathbf{I}_\perp = ehM_P \mathbf{E}_\perp n - ehM_H \frac{\mathbf{E}_\perp \times \mathbf{B}_0}{|\mathbf{B}_0|} n. \quad (3)$$

[13] The response equation is expressed by [Sato, 1978; Miura and Sato, 1980, Appendix A]

$$\nabla_\perp^2 \Phi_{IS} (= -\nabla_\perp \cdot \mathbf{E}_\perp) = -Zj_\parallel. \quad (4)$$

[14] Here,  $\mathbf{E}_\perp$ ,  $\mathbf{B}_0$ , and  $n$  are the ionospheric electric field, the geomagnetic field, and the ionospheric plasma number density, respectively;  $j_\parallel$  is the field-aligned current density at the ionosphere height;  $e$  is the electronic charge;  $h$  is the effective height range of the ionospheric region of interest;  $\alpha$  is the recombination coefficient;  $M_P$  and  $M_H$  are the Pedersen and Hall mobilities, respectively;  $\Phi_{IS}$  is the ionospheric electric potential;  $Z$  is the magnetospheric impedance. The subscript  $\perp$  refers to quantities or operators which are on the perpendicular surface to the geomagnetic field. We assume the Cartesian coordinates as shown in Figure 2, that is, the positive  $x$  axis is directed upward along the field line, the positive  $y$  axis toward the equator, and the positive  $z$  axis toward the east. Further, we suppose that the ionospheric electric field induced by the convection flow and the region 1 current system are constant and that they satisfy the above equations.

[15] Next, we consider the small difference from this equilibrium state. Here, we assume that the longitudinal difference is negligible, i.e.,  $\partial/\partial z \ll \partial/\partial y$ . Thus, the ionospheric electrostatic waves can only propagate along the  $y$  axis and the perturbed component of  $E_z$  does not arise. Omitting second order terms, we can rewrite equations (1)–(4) as

$$\frac{\partial n_1}{\partial t} = \frac{j_{\parallel 1}}{eh} - 2\alpha n_0 n_1, \quad (5)$$

$$\frac{\partial I_{y1}}{\partial y} = -j_{\parallel 1}, \quad (6)$$

$$I_{y1} = ehM_P(E_{y0}n_1 + E_{y1}n_0) + ehM_H E_{z0}n_1, \quad (7)$$

$$\frac{\partial E_{y1}}{\partial y} = Zj_{\parallel 1}, \quad (8)$$

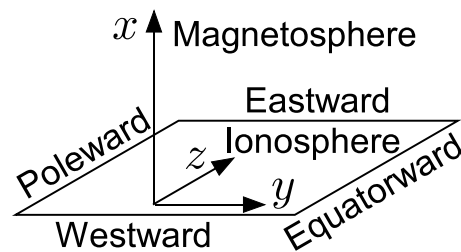


**Figure 2.** Schematic diagram of system for theoretical model.

where the reference frame moves with the electric drift velocity,  $V_{E \times B}^y = -E_{z0}/|B_0|$ , in the  $y$  direction. The subscripts 0 and 1 indicate equilibrium and perturbed quantities, respectively.

[16] Assuming that the perturbed quantities are proportional to  $\exp[i(\omega t - ky)]$ , we find that linearization of equations (5)–(8) yields the dispersion relation as

$$\omega = \frac{1 + \sigma}{1 + \frac{Z}{R}} M_P E_{y0} k + 2i\alpha n_0, \quad (9)$$

where  $\sigma$  and  $R$  are defined by

$$\sigma = \frac{M_H E_{z0}}{M_P E_{y0}}, \quad (10)$$

$$R = \frac{1}{ehM_P n_0}, \quad (11)$$

respectively. The magnetospheric impedance  $Z$  is approximately given by [Sato, 1978; Miura and Sato, 1980]

$$Z = -i\mu_0 v_A \cot(k_{\parallel} l), \quad (12)$$

where  $\mu_0$  is the permeability;  $v_A$  is the Alfvén speed;  $k_{\parallel}$  is the wave number of the Alfvén wave propagating along the magnetic field;  $l$  is the length of the field line from the ionosphere to the magnetospheric equator;  $\pi/2 < k_{\parallel} l < \pi$ . From equations (9) and (12), we obtain

$$\text{Re}(\omega) \equiv \Omega = \frac{1}{1 + \zeta^2} (1 + \sigma) M_P E_{y0} k, \quad (13)$$

$$-\text{Im}(\omega) \equiv \Gamma = \frac{\zeta}{1 + \zeta^2} (1 + \sigma) M_P E_{y0} k - 2\alpha n_0, \quad (14)$$

where,

$$\zeta = \frac{\text{Im}(Z)}{R} = -\frac{\mu_0 v_A}{R} \cot(k_{\parallel} l). \quad (15)$$

[17] Because  $\Omega > 0$ , the ionospheric electrostatic wave propagates to the direction of  $E_{y0}$  when  $\sigma > -1$ .

[18] At any  $k$ , equation (14) indicates that the growth rate of the feedback instability,  $\Gamma$ , has a maximum value,  $\Gamma_{\max}$ , when  $\zeta = 1$ .

[19] On the other hand, since  $\Omega$  is also the frequency of the magnetospheric Alfvén wave,  $\Omega$  at  $\Gamma = \Gamma_{\max}$  (i.e.,  $\zeta = 1$ ) can be given as

$$\begin{aligned} \Omega_{\max} &= v_A k_{\parallel} \\ &= \frac{v_A}{l} \cot^{-1} \left( -\frac{R}{\mu_0 v_A} \right). \end{aligned} \quad (16)$$

[20] Using equations (13) and (16), we obtain the maximum growth rate as

$$\begin{aligned} \Gamma_{\max} &= \Omega_{\max} - 2\alpha n_0 \\ &= \frac{v_A}{l} \cot^{-1} \left( -\frac{R}{\mu_0 v_A} \right) - 2\alpha n_0. \end{aligned} \quad (17)$$

## 2.2. Effects of Non-Uniform Electric Field and Plasma Density

[21] So far, while the dependence of the feedback instability on an equilibrium ionospheric background conductivity which is spatially uniform has been studied by many authors [e.g., Lysak, 1986, 1991], the effects of gradients of equilibrium ionospheric electric field and conductivity have been ignored in many cases. Here, we consider the effects of the non-uniform ionospheric electric field and the non-uniform ionospheric plasma density. In order to investigate these effects,  $\partial E_{y0}/\partial y$  and  $\partial n_0/\partial y$  (i.e., the spatial non-uniformity of the equilibrium quantities) are not removed at substitution of equation (7) into equation (6). Then, we obtain

$$\omega = \frac{1 + \sigma + i\varepsilon}{1 + \frac{Z}{R}(1 + i\nu)} M_P E_{y0} k + 2i\alpha n_0, \quad (18)$$

where  $\varepsilon$  and  $\nu$  are defined by

$$\varepsilon = \frac{1}{kE_{y0}} \frac{\partial E_{y0}}{\partial y}, \quad (19)$$

$$\nu = \frac{1}{kn_0} \frac{\partial n_0}{\partial y}, \quad (20)$$

respectively. From equations (12) and (18), we obtain

$$\text{Re}(\omega) \equiv \Omega = F(\tilde{\varepsilon}, \nu, \zeta) (1 + \sigma) M_P E_{y0} k, \quad (21)$$

$$-\text{Im}(\omega) \equiv \Gamma = G(\tilde{\varepsilon}, \nu, \zeta) (1 + \sigma) M_P E_{y0} k - 2\alpha n_0, \quad (22)$$

where,

$$F(\tilde{\varepsilon}, \nu, \zeta) = \frac{1 + (\tilde{\varepsilon} - \nu)\zeta}{1 - 2\nu\zeta + (1 + \nu^2)\zeta^2}, \quad (23)$$

$$G(\tilde{\varepsilon}, \nu, \zeta) = \frac{(1 + \tilde{\varepsilon}\nu)\zeta - \tilde{\varepsilon}}{1 - 2\nu\zeta + (1 + \nu^2)\zeta^2}, \quad (24)$$

$$\tilde{\varepsilon} = \frac{\varepsilon}{1 + \sigma}. \quad (25)$$

Because  $\Omega > 0$ , the ionospheric electrostatic wave propagates to the direction of  $E_{y0}$  when  $F(\tilde{\varepsilon}, \nu, \zeta) > 0$  and  $\sigma > -1$ .

[22] At any  $k$ , equation (22) indicates that the growth rate of the feedback instability,  $\Gamma$ , has a maximum value when  $G$  also is maximum. When  $G$  becomes maximum,  $\zeta$  are given by

$$\zeta_{\max} = \frac{1}{1 + \tilde{\varepsilon}\nu} \left( \tilde{\varepsilon} + \sqrt{\frac{1 + \tilde{\varepsilon}^2}{1 + \nu^2}} \right). \quad (26)$$

Here, we show the dependence of  $\zeta_{\max}$  on  $\tilde{\varepsilon}$  and  $\nu$  in Figure 3a. This panel indicates that  $\zeta_{\max}$  increases with increasing  $\tilde{\varepsilon}$ , that is, the magnetospheric inductance which is required for the field-aligned current growth decreases with decreasing  $\tilde{\varepsilon}$ . This fact means that the instability arises more frequently at the smaller  $\tilde{\varepsilon}$ .

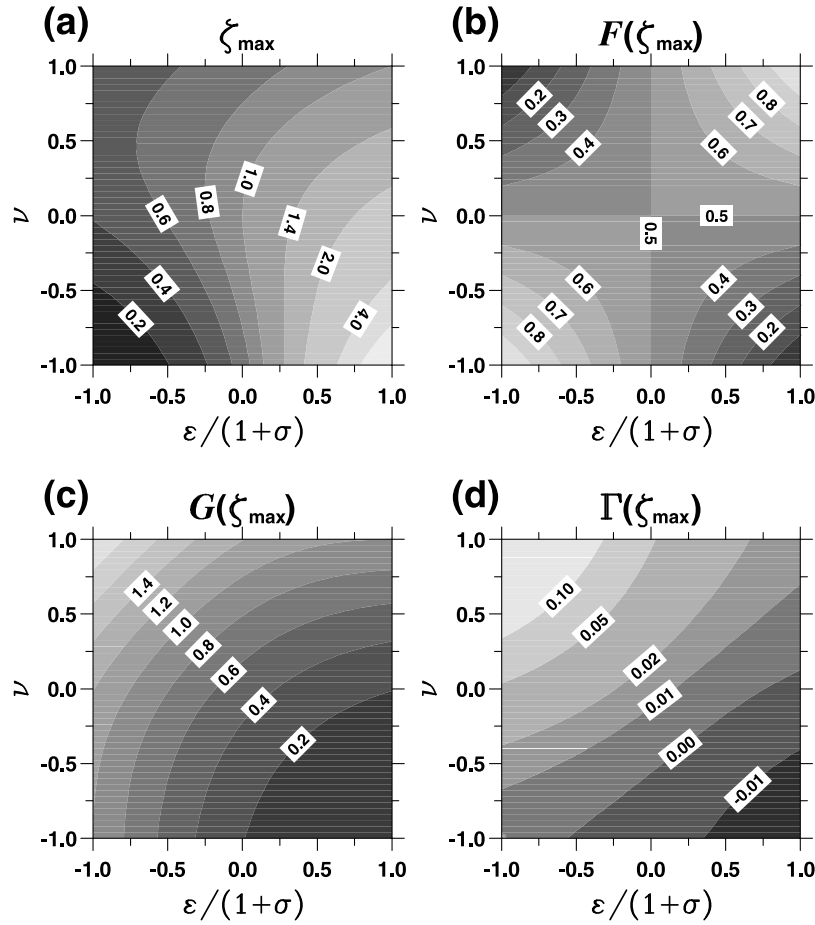


**Figure 3.** Dependence of quantities (a)  $\zeta_{\max}$ , (b)  $F(\zeta_{\max})$ , (c)  $G(\zeta_{\max})$ , and (d)  $\Gamma(\zeta_{\max})$  on  $\tilde{\varepsilon}$  and  $\nu$ .

[23] From Figure 3b which represents the dependence of  $F(\zeta_{\max})$  on  $\tilde{\varepsilon}$  and  $\nu$ , we find that  $F(\zeta_{\max}) > 0$  in the region of  $|\tilde{\varepsilon}| < 1$  and  $|\nu| < 1$ . Accordingly, the ionospheric electrostatic wave propagates to the direction of  $E_{y0}$  at  $\zeta = \zeta_{\max}$ .

[24] Further, Figure 3c shows the dependence of  $G(\zeta_{\max})$  on  $\tilde{\varepsilon}$  and  $\nu$ . Figure 3c indicates that  $G(\zeta_{\max})$  becomes larger as  $\tilde{\varepsilon}$  decreases or as  $\nu$  increases. This is explained by using a following equation:

$$\begin{aligned} \frac{\partial n_1}{\partial t} = & -M_P n_1 \frac{\partial E_{y0}}{\partial y} - M_P E_{y1} \frac{\partial n_0}{\partial y} \\ & - (M_P E_{y0} + M_H E_{z0}) \frac{\partial n_1}{\partial y} \\ & - M_P n_0 \frac{\partial E_{y1}}{\partial y} - 2\alpha n_0 n_1, \end{aligned} \quad (27)$$

which is derived from the elimination of  $j_{\parallel 1}$  from equations (5)–(7). The first term in the right-hand side of equation (27) indicates that the growth rate increases as  $\varepsilon$  decreases. The phase difference between  $E_{y1}$  in the second term in the right-hand side of equation (27) and  $n_1$  must be  $\pi$  (or 0) in the case of  $k > 0$  (or  $k < 0$ ). Consequently, at  $k > 0$  (or  $k < 0$ ), the growth rate increases with increasing (or decreasing)  $\partial n_0 / \partial y$ , that is, increasing  $\nu$ .

[25] On the other hand,  $\Omega$  can be given as

$$\begin{aligned} \Omega = & v_A k_{\parallel} \\ = & \frac{v_A}{l} \cot^{-1} \left( -\zeta \frac{R}{\mu_0 v_A} \right). \end{aligned} \quad (28)$$

Thus, the wave number  $k$  should satisfy

$$F(\tilde{\varepsilon}, \nu, \zeta)(1 + \sigma) M_P E_{y0} k = \frac{v_A}{l} \cot^{-1} \left( -\zeta \frac{R}{\mu_0 v_A} \right). \quad (29)$$

Using equations (21) and (28), we can rewrite equation (22) as

$$\begin{aligned} \Gamma = & \frac{G(\tilde{\varepsilon}, \nu, \zeta)}{F(\tilde{\varepsilon}, \nu, \zeta)} \Omega - 2\alpha n_0 \\ = & \frac{G(\tilde{\varepsilon}, \nu, \zeta) v_A}{F(\tilde{\varepsilon}, \nu, \zeta) l} \cot^{-1} \left( -\zeta \frac{R}{\mu_0 v_A} \right) - 2\alpha n_0. \end{aligned} \quad (30)$$

[26] Figure 3d shows the dependence of  $\Gamma(\zeta_{\max})$  on  $\tilde{\varepsilon}$  and  $\nu$ . Here,  $\Gamma(\zeta_{\max})$  is obtained by substitution of  $\zeta = \zeta_{\max}$  into equation (30). The parameters in Figure 3d are as follows. The Alfvén speed is  $v_A = 1.0 \times 10^6$  [ms<sup>-1</sup>]. The length of the field line is  $l = 7.2 \times 10^7$  [m]. The effective height of the ionosphere is  $h = 1.2 \times 10^4$  [m]. The Pedersen mobility is  $M_P = 1.6 \times 10^4$  [m<sup>2</sup> s<sup>-1</sup> V<sup>-1</sup>]. The recombination coefficient

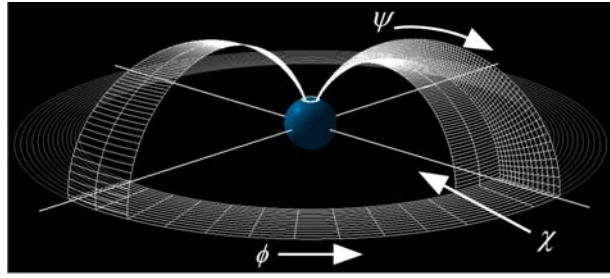


**Figure 4.** Schematic view showing grid system.

is  $\alpha = 3.0 \times 10^{-13} [\text{m}^3 \text{s}^{-1}]$ . The equilibrium ionospheric plasma density is  $n_0 = 3.0 \times 10^{10} [\text{m}^{-3}]$ . This panel also shows a trend similar to that in Figure 3c.

### 2.3. Effect of Non-Uniform Field Line Length

[27] Actually, because  $l$  depends on  $y$ , i.e., on the latitude, propagating waves may go into the region where the growth condition is not satisfied. In order to investigate the effect of the spatially non-uniform  $l$  on the instability, we consider the change of  $k$  with propagation of a wave which has a constant frequency  $\Omega_0 = v_A k_{\parallel 0}$ . From equation (21), the wave number of the ionospheric electrostatic wave is given as

$$k = \frac{\Omega_0}{F(\tilde{\varepsilon}, \nu, \zeta)(1 + \sigma)M_P E_{y0}}. \quad (31)$$

Thus, the derivative of  $k$  with respect to  $y$  is obtained as

$$\begin{aligned} \frac{\partial k}{\partial y} = & \left\{ 2[(1 + \nu^2)\zeta - \nu]F(\tilde{\varepsilon}, \nu, \zeta) - \tilde{\varepsilon} + \nu \right\} \\ & \times \left[ \left( \frac{\mu_0 v_A}{R} + \frac{R}{\mu_0 v_A} \zeta^2 \right) k_{\parallel 0} \frac{\partial l}{\partial y} + k \nu \zeta \right] \\ & - k \tilde{\varepsilon} [1 + (\varepsilon - \nu)\zeta] \left\{ \frac{k}{1 + (\tilde{\varepsilon} - \nu)\zeta} \right\}, \end{aligned} \quad (32)$$

where the dependence of  $\varepsilon$  and  $\nu$  on  $y$  is neglected. Particularly, when  $\varepsilon = 0$  and  $\nu = 0$ , equation (32) is rewritten as

$$\frac{\partial k}{\partial y} = \frac{2\zeta k}{1 + \zeta^2} \left( \frac{\mu_0 v_A}{R} + \frac{R}{\mu_0 v_A} \zeta^2 \right) k_{\parallel 0} \frac{\partial l}{\partial y}. \quad (33)$$

From equation (33), we have the change rate of  $k$  per unit time as

$$\begin{aligned} \frac{1}{k} \frac{\partial k}{\partial t} &= \frac{1}{k} \frac{\partial y}{\partial t} \frac{\partial k}{\partial y} \\ &= \frac{1}{k} \frac{\Omega_0}{k} \frac{\partial k}{\partial y} = (1 + \sigma) M_P E_{y0} k_{\parallel 0} \frac{\partial l}{\partial y} \\ &\quad \times \left[ \frac{2\zeta}{1 + \zeta^2} \left( \frac{\mu_0 v_A}{R} + \frac{R}{\mu_0 v_A} \zeta^2 \right) \right]. \end{aligned} \quad (34)$$

This change rate becomes maximum at

$$\zeta = \left[ \frac{3}{2} \left( 1 - \frac{\mu_0^2 v_A^2}{R^2} \right) + \sqrt{\frac{9}{4} \left( 1 - \frac{\mu_0^2 v_A^2}{R^2} \right)^2 + \frac{\mu_0^2 v_A^2}{R^2}} \right]^{1/2}. \quad (35)$$

By using the same parameters as in Figure 3d, equation (35) yields  $\zeta = 0.87$ . Since  $\zeta_{\max} = 1$  when  $\varepsilon = 0$  and  $\nu = 0$ , the change rate of  $k$  is larger at the vicinity of  $\zeta_{\max}$ . Assuming that  $\zeta = 1$ ,  $\sigma = 0$ ,  $E_{y0} = -0.1 [\text{V/m}]$ ,  $\partial l / \partial y = -8 \times 10$ ,  $k_{\parallel 0} l \sim 2$ , and  $l = 7.2 \times 10^7 [\text{m}]$ , the absolute value of  $k$  increases by 0.36% per unit time. In other words,  $|k|$  increases twice per about 200 s. Because of such a dependence of  $l$  on the latitude,  $\zeta$  may be smaller than  $\zeta_{\max}$  in actual waves. And then, from equations (22) and (24), it is expected that the growth rate decreases with decreasing  $\zeta$ .

## 3. Simulation Studies

[28] We now study the quiet auroral arc formation by the feedback instability in such a realistic system as has a dipole geomagnetic field by means of a three-dimensional MHD simulation code. In this section, we mention the numerical model of the three-dimensional dipole M-I coupling system and show the results of the simulation runs.

### 3.1. Model and Procedure

[29] In our simulation code, we adopted the three-dimensional dipole coordinates [Kageyama *et al.*, 2006] in order to express a dipole geomagnetic field. The simulation region is confined by the ionospheric auroral zone (the region 1 auroral oval) which is from the latitude  $70.0^\circ$  to  $72.3^\circ$ , the magnetospheric equatorial plane, and surfaces which are made from the geomagnetic field lines connected to the poleward and equatorward boundaries of the auroral zone.

[30] Here, we define  $\psi$  as the direction from the ionosphere to the magnetospheric equator along the geomagnetic field,  $\chi$  as the direction toward the equator along the meridian, and  $\phi$  as the direction toward the east along the parallel of latitude. The grid numbers in the  $\psi$ ,  $\chi$ , and  $\phi$  directions are 1279, 66, and 256, respectively. Figure 4 is the schematic view which represents the simulation region and the grid system.

[31] Magnetospheric dynamics are described by one-fluid MHD equations,

$$\frac{\partial \mathbf{B}}{\partial t} = -\nabla \times \mathbf{E}, \quad (36)$$

$$\frac{\partial(\rho_0 \mathbf{v})}{\partial t} = -\nabla \cdot (\rho_0 \mathbf{v} \mathbf{v}) + \mathbf{j} \times \mathbf{B}, \quad (37)$$

$$\mathbf{E} = -\mathbf{v} \times \mathbf{B}, \quad (38)$$

$$\mu_0 \mathbf{j} = \nabla \times \mathbf{B}, \quad (39)$$

where  $\mathbf{B}$ ,  $\mathbf{E}$ ,  $\mathbf{v}$ ,  $\mathbf{j}$ , and  $\rho$  are the magnetic field, the electric field, the velocity of the plasma flow, the current density, and the mass density, respectively. The mass density  $\rho$  is supposed to be constant as  $\rho = \rho_0$  where  $\rho_0$  is given as Alfvén speed  $v_A$  is spatially uniform (the validity of this assumption is discussed by Watanabe *et al.* [1993]).

[32] The dipole geomagnetic field is given by

$$\begin{aligned} B_{\psi 0}(\psi, \chi) &= \left( \frac{1 + 3 \cos^2[\theta(\psi, \chi)]}{1 + 3 \cos^2[\theta(0, \chi_{\text{mid}})]} \right)^{1/2} \\ &\quad \times \left( \frac{R_E}{|\mathbf{r}(\psi, \chi)|} \right)^3 B_{\text{IS}}. \end{aligned} \quad (40)$$



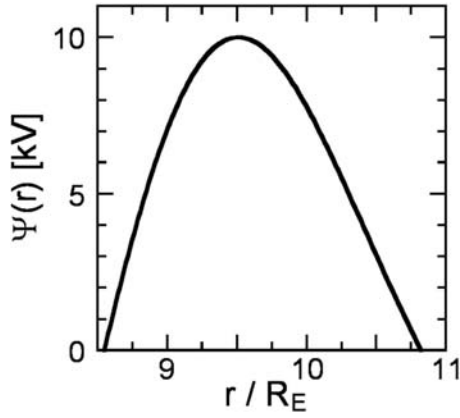


**Figure 5.** Profile of the equatorial potential.

Here,  $R_E$  is the earth radius;  $\mathbf{r}$  is the radius vector from the center of the earth to an arbitrary point;  $\theta$  is the angle between the polar axis and  $\mathbf{r}$ ; “ $\psi = 0$ ” refers to the boundary at the ionosphere;  $\chi_{\text{mid}}$  represents the midpoint in the  $\chi$  direction in the simulation region;  $B_{\text{IS}}$  is the geomagnetic field at the ionosphere height as  $B_{\text{IS}} = B_{\psi 0}(0, \chi_{\text{mid}})$ .

[33] At the latitudinal boundaries, any plasma flows, electric currents, and Alfvén waves across the boundaries are prohibited. Accordingly, the boundary conditions at  $\chi = \chi_{\text{max}}$  and  $\chi = \chi_{\text{min}}$  are given by [Watanabe et al., 1986]

$$B_\chi = 0, \quad (41)$$

$$(\nabla \times \mathbf{B})_\psi = 0, \quad (42)$$

$$(\nabla \times \mathbf{B})_\phi = 0, \quad (43)$$

$$v_\chi = 0, \quad (44)$$

$$(\nabla \times \mathbf{v})_\psi = 0, \quad (45)$$

$$(\nabla \times \mathbf{v})_\phi = 0. \quad (46)$$

[34] At the magnetospheric equatorial plane, a twin-vortex convection flow is supplied permanently as a boundary condition. This plasma convection sustains a region 1 current system (see Figure 1). The convection flow

velocity and the consistent equatorial electric field are produced by an equatorial potential,

$$\Phi_{\text{Eq}}(\chi, \phi) = -\Psi(r) \sin \phi, \quad (47)$$

where  $r = |\mathbf{r}(\psi_{\text{max}}, \chi)|$ ; “ $\psi = \psi_{\text{max}}$ ” refers to the boundary at the magnetospheric equator; “ $\phi = 0$  (or  $\phi = 2\pi$ )” represents the direction to the sun (i.e., 12:00 local time). The profile of  $\Psi(r)$  is presented in Figure 5. It is supposed that the maximum of the equatorial potential is 10 kV as shown in Figure 5. The potential profile  $\Psi(r)$  is obtained numerically as it satisfies equations (44) and (45) at  $\chi = \chi_{\text{max}}$  and  $\chi = \chi_{\text{min}}$ . Further, we assume that  $\partial \mathbf{B} / \partial t = 0$  at  $\psi = \psi_{\text{max}}$ .

[35] At the ionospheric boundary ( $\psi = 0$ ), the elliptic partial differential equation of  $\Phi_{\text{IS}}$ ,

$$\nabla_\perp \cdot \left( ehM_{\text{pn}}(\nabla_\perp \Phi_{\text{IS}}) + ehM_{\text{Hn}} \frac{\mathbf{B}_0 \times (\nabla_\perp \Phi_{\text{IS}})}{|\mathbf{B}_0|} \right) = j_\parallel, \quad (48)$$

which is obtained by substitution of equation (3) into equation (2) is solved every time step. Here,  $j_\parallel$  is given as  $j_\parallel = j_\psi(0, \chi, \phi)$ . And then, the electric field  $\mathbf{E}(0, \chi, \phi)$  and the flow velocity  $\mathbf{v}(0, \chi, \phi)$  are supplied as

$$\mathbf{E}(0, \chi, \phi) = -\nabla_\perp \Phi_{\text{IS}}(\chi, \phi), \quad (49)$$

and

$$\mathbf{v}(0, \chi, \phi) = -\frac{[\nabla_\perp \Phi_{\text{IS}}(\chi, \phi)] \times \mathbf{B}_0}{|\mathbf{B}_0|^2}, \quad (50)$$

respectively.

[36] Additionally, the time evolution of the ionospheric plasma density is calculated by integration of the ionospheric plasma density continuity equation,

$$\frac{\partial n}{\partial t} = -\frac{\mathbf{E}_\perp \times \mathbf{B}_0}{|\mathbf{B}_0|^2} \cdot \nabla_\perp n + \frac{j_\parallel}{eh} - \alpha(n^2 - n_0^2). \quad (51)$$

Here, it is assumed that ionospheric cold electrons would not escape to the magnetosphere. Accordingly, the  $j_\parallel$  term in equation (51) is only considered at  $j_\parallel > 0$ . Since the ionospheric plasma density depends on time, the ionospheric Pedersen and Hall conductivities ( $ehM_{\text{pn}}$  and  $ehM_{\text{Hn}}$ ) also change temporally.

[37] These governing equations are transformed into the finite difference equations. Time integration is carried out by the forth-order Runge-Kutta-Gill (RKG) method [Watanabe and Sato, 1990].

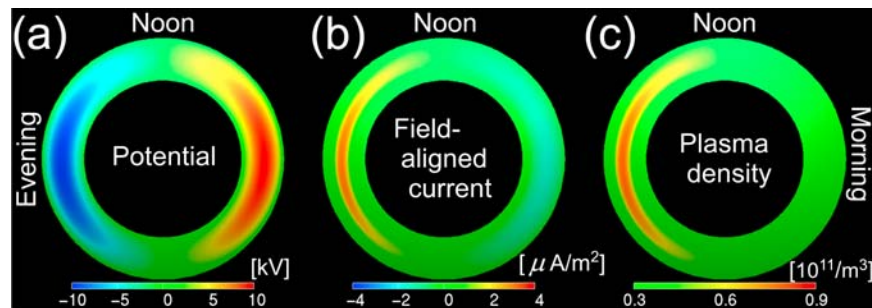


**Figure 6.** (a) Potential, (b) field-aligned current density, and (c) plasma density distributions at the ionosphere height at the quasi-steady state.

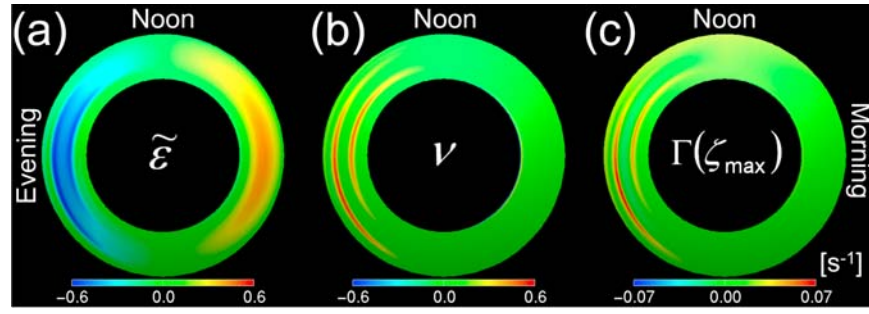


**Figure 7.** Distributions of quantities (a)  $\tilde{\epsilon}$ , (b)  $\nu$ , and (c)  $\Gamma(\zeta_{\max})$ . These are calculated from the quasi-steady state data.

[38] The simulation parameters are as follows. The Alfvén speed is  $v_A = 1.0 \times 10^6$   $[ms^{-1}]$ . The geomagnetic field strength at the ionosphere height is  $B_{IS} = -3.1 \times 10^{-5}$   $[T]$ . The earth radius is  $R_E = 6.37 \times 10^6$   $[m]$ . The effective height of the ionosphere is  $h = 1.2 \times 10^4$   $[m]$ . The recombination coefficient is  $\alpha = 3.0 \times 10^{-13}$   $[m^3 s^{-1}]$ . The Pedersen and Hall mobilities are  $M_P = 1.6 \times 10^4$   $[m^2 s^{-1} V^{-1}]$  and  $M_H = 3.2 \times 10^4$   $[m^2 s^{-1} V^{-1}]$ , respectively. The initial ionospheric plasma density is uniform as  $n_{ini} = 3.0 \times 10^{10}$   $[m^{-3}]$ . Thus, the initial ionospheric Pedersen and Hall conductivities ( $eM_P n_{ini}$  and  $eM_H n_{ini}$ ) are also uniform. The time step is  $\Delta t = 2.9 \times 10^{-3}$   $[s]$ .

[39] Here, we define the Alfvén transit time  $\tau_A$  which is the time for propagation of an Alfvén wave from the magnetospheric equator to the ionosphere. In this paper,  $\tau_A = l_{\max}/v_A = 88.7$   $[s]$  where  $l_{\max}$  is the length of the geomagnetic field line between  $\psi = 0$  and  $\psi = \psi_{\max}$  at  $\chi = \chi_{\min}$ .

### 3.2. Simulation Results

[40] First, we solved the governing equations without the time evolution of the ionospheric plasma density (i.e., equation (51)) for 2,636 s ( $\approx 30\tau_A$ ). Next, supplementing equation (1), we computed the evolution for 527 s ( $\approx 6\tau_A$ ). Consequently, we have the quasi-steady state as shown in Figure 6. Figures 6a, 6b, and 6c represent the distributions of the ionospheric electric potential, the field-aligned current density at the ionosphere height, and the ionospheric plasma density, respectively. Since the actual latitudinal width of the simulation region is very narrow (2.3 degrees), the width in Figure 6 is widened to 8.3 degrees. Figures 6a–6c indicate that Heppner’s potential pattern and a region 1 current system are formed. Also, by using the quasi-steady state data, the distributions of  $\tilde{\epsilon}$ ,  $\nu$ , and  $\Gamma(\zeta_{\max})$  can be obtained as shown in Figure 7.

[41] Now, with addition of random small perturbations, the M-I coupling dynamics has been evolved. Figure 8 shows the distributions of the field-aligned current density perturbation at the ionosphere height (Figure 8a) and the ionospheric plasma density perturbation (Figure 8b) at  $t = 3,662$  s ( $\approx 41\tau_A$ ). Here,  $t$  is the time from the quasi-steady state and these perturbed quantities are the difference from those of the quasi-steady state. In these panels, we find that some longitudinally striated structures are developed. Particularly, the structure around 19:00 local time and 70.5° latitude is more intensive. This trend coincides with that of the theoretical growth rate distribution as shown in Figure 7c.

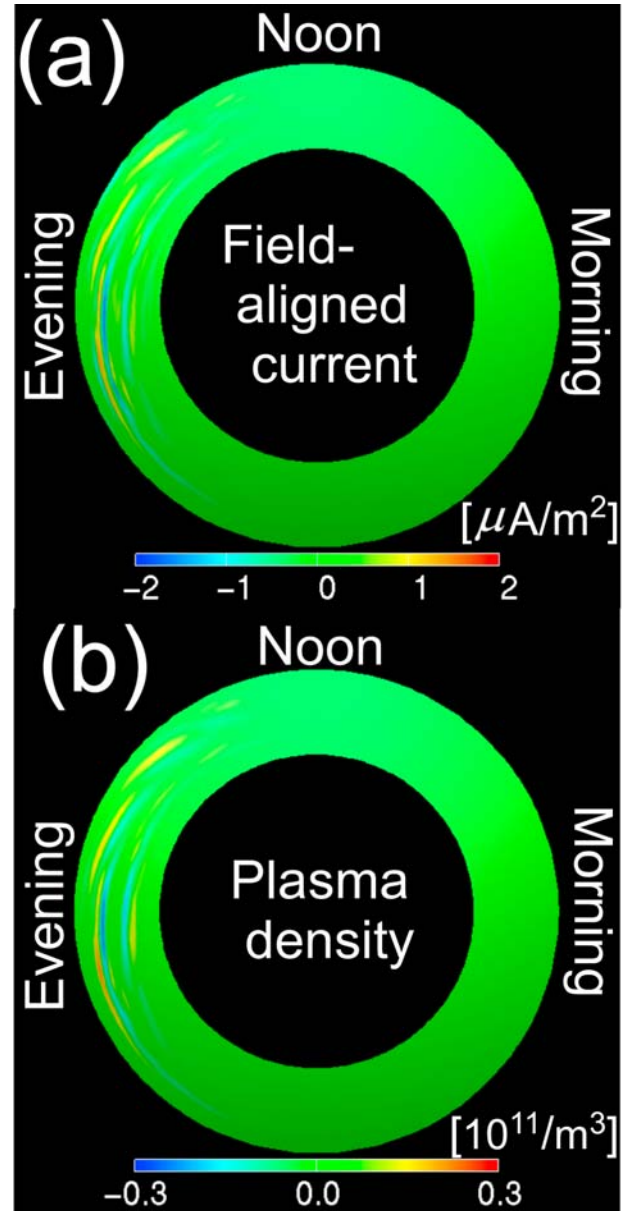


**Figure 8.** Distributions of (a) the field-aligned current density perturbation at the ionosphere height and (b) the ionospheric plasma density perturbation at  $t = 3,662$  s. Here,  $t$  is the time from the quasi-steady state.



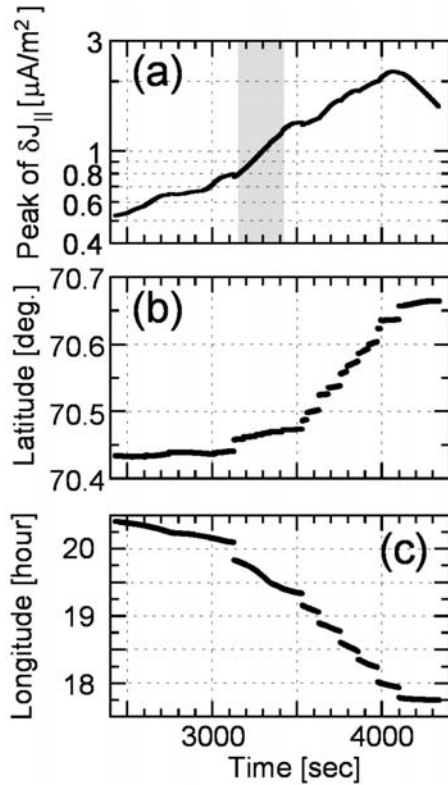


**Figure 9.** Time variations of (a) the amplitude, (b) the latitude, and (c) the longitude of a field-aligned current density peak at the ionosphere height.

[42] Figure 9 presents the time variations of the field-aligned current amplitude (Figure 9a), the latitude (Figure 9b), and the longitude (Figure 9c) of a peak in a longitudinally striated structure. In Figure 9a, the linear exponential growth with the growth rate of  $1.6 \times 10^{-3} \text{ s}^{-1}$  is observed in the shaded time span. Although the observed growth rate is smaller than the theoretical maximum one ( $\sim 7 \times 10^{-2} \text{ s}^{-1}$ ), this is probably due to the effects of the nonlinear recombination ( $-\alpha n_1 = -4.5 \times 10^{-3} \text{ s}^{-1}$ ) and the non-uniform  $I$ . Furthermore, from Figures 9b and 9c, it is found that the perturbation moves polar-westward with the latitudinal velocity of  $\sim 1.6 \times 10 \text{ m/s}$  and the longitudinal velocity of  $\sim 9.2 \times 10^2 \text{ m/s}$ , which is consistent with the Pedersen (poleward) and Hall (westward) drift for the poleward electric field at the position of the perturbation. This fact also coincides with the theory [Sato, 1978]. Then, the growth of this peak stagnates when it reaches to the limit of the unstable region where the color becomes more red-dish in Figure 7c.

[43] Figures 10 and 11 show the results for the case that the Pedersen mobility is taken to be  $M_P = 3.2 \times 10^4 \text{ [m}^2 \text{ s}^{-1} \text{ V}^{-1}]$ , i.e., two times as large as  $M_P$  in the above original case. Figure 10 displays the distributions of the field-aligned current density perturbation at the ionosphere height (Figure 10a) and the ionospheric plasma density perturbation (Figure 10b) at  $t = 3,662 \text{ s}$  ( $\approx 41\tau_A$ ). Further, we show the time variation of the field-aligned current amplitude of a peak in a longitudinally striated structure in Figure 11. The comparison of Figures 8 and 10 indicates that the number of longitudinally striated structures and the

amplitude of perturbations in the present case are larger than those in the previous case. Also, the growth rate of the linear exponential growth in the shaded time span in Figure 11 is observed as  $4.6 \times 10^{-3} \text{ s}^{-1}$ , which is about three times as large as one in the previous case. These results are consistent with the theory which predicts that the growth rate would increase with  $M_P$  increasing (see equation (22)).

#### 4. Summary and Discussion

[44] We have studied quiet auroral arcs formation by means of the MHD simulation of the three-dimensional dipole M-I coupling system. It has been shown that some

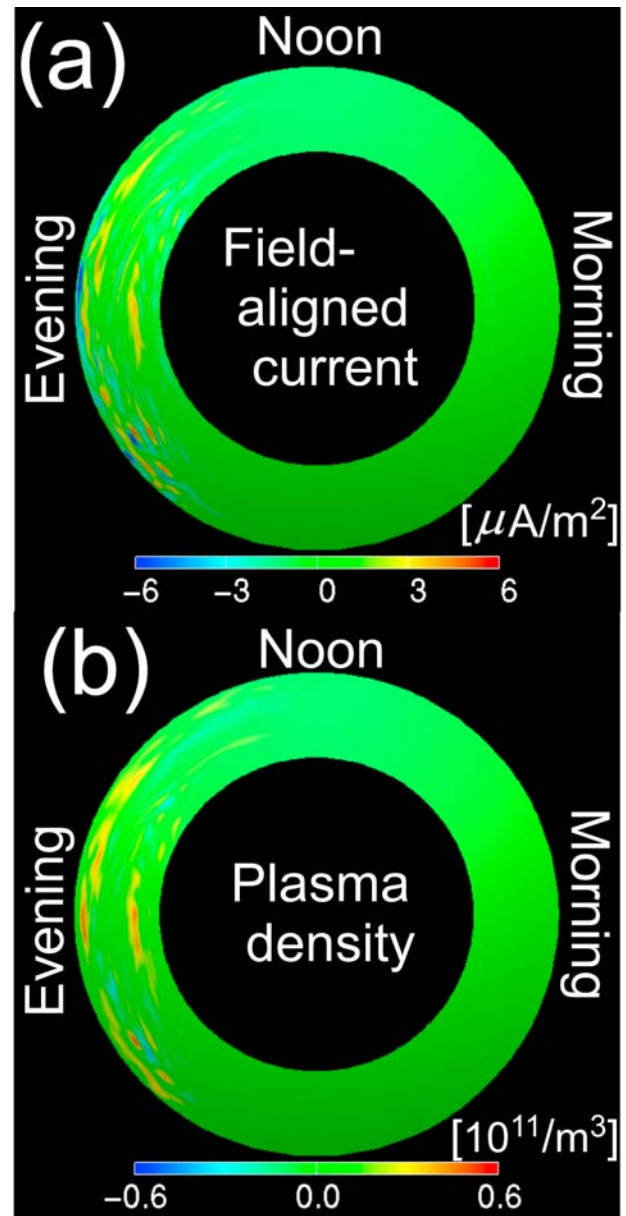


**Figure 10.** Result of the simulation for  $M_P = 3.2 \times 10^4 \text{ [m}^2 \text{ s}^{-1} \text{ V}^{-1}]$ . This figure shows distributions of (a) the field-aligned current density perturbation at the ionosphere height and (b) the ionospheric plasma density perturbation at  $t = 3,662 \text{ s}$ . Here,  $t$  is the time from the quasi-steady state.

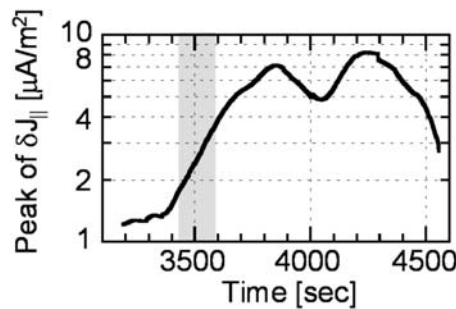


**Figure 11.** Result of the simulation for  $M_p = 3.2 \times 10^4$  [ $\text{m}^2 \text{s}^{-1} \text{V}^{-1}$ ]. Figure 11 shows the time variation of the amplitude of a field-aligned current density peak at the ionosphere height.

longitudinally striated structures are formed and developed by the feedback instability in such a realistic system. The areas where these structures appear are consistent with the prediction by the integrated feedback theory which includes the effects of the spatially non-uniform ionospheric electric field and non-uniform ionospheric plasma number density. From the difference between the theoretically predicted and the observed growth rates, it is inferred that the effect of the non-uniform field line length is not negligible.

[45] Although Figures 8a and 10a show that there are downward perturbations on the side of upward perturbations, downward (return) current regions are little in the total current distribution. The production of the return current on the side of upward current as observed by rockets [Park and Cloutier, 1971; Casserly and Cloutier, 1975; Robinson *et al.*, 1981] requires more growth of the current perturbation. In this process, microscopic phenomena are expected to play an important role. Actually, when the upward current (downward electron flow) grows and exceeds a certain threshold, the electric potential difference (anomalous resistivity) along the magnetic field is thought to be generated by the ion-acoustic instability [Sato and Okuda, 1980]. Then, auroral energetic electrons (1 keV  $\sim$ ) accelerated by this potential difference ionize ionospheric neutral particles. This growth of the ionospheric plasma density probably modifies the ionospheric electric field and the field-aligned current. In our following paper (H. Hasegawa *et al.*, Holistic simulation of quiet auroral arcs formation, manuscript in preparation, 2010), the MMI simulation model that includes the above microscopic process is presented and the effect of accelerated electrons on the quiet auroral arcs formation is discussed with the results of MMI simulations.

[46] **Acknowledgments.** The authors would like to thank Drs. A. Kageyama, T. Sugiyama, K. Kusano, and S. Hirose for their valuable discussions. The simulation was carried out on the Earth Simulator/JAMSTEC.

[47] Robert Lysak thanks the reviewers for their assistance in evaluating this paper.

## References

Atkinson, G. (1970), Auroral arcs: Result of the interaction of a dynamic magnetosphere with the ionosphere, *J. Geophys. Res.*, **75**(25), 4746–4755.

- Casserly, R. T., Jr., and P. A. Cloutier (1975), Rocket-based magnetic observations of auroral Birkeland currents in association with a structured auroral arc, *J. Geophys. Res.*, **80**(16), 2165–2168.
- Chaston, C. C., V. Genot, J. W. Bonnell, C. W. Carlson, J. P. McFadden, R. E. Ergun, R. J. Strangeway, E. J. Lund, and K. J. Hwang (2006), Ionospheric erosion by Alfvén waves, *J. Geophys. Res.*, **111**, A03206, doi:10.1029/2005JA011367.
- Heppner, J. P. (1977), Empirical models of high-latitude electric field, *J. Geophys. Res.*, **82**(7), 1115–1125.
- Holzer, T. E., and T. Sato (1973), Quiet auroral arcs and electrodynamic coupling between the ionosphere and the magnetosphere, 2, *J. Geophys. Res.*, **78**(31), 7330–7339.
- Iijima, T., and T. A. Potemra (1976), The amplitude distribution of field-aligned currents at northern high latitudes observed by triad, *J. Geophys. Res.*, **81**(13), 2165–2174.
- Kageyama, A., T. Sugiyama, K. Watanabe, and T. Sato (2006), A note on the dipole coordinates, *Comput. Geosci.*, **32**, 265–269, doi:10.1016/j.cageo.2005.06.006.
- Kozlovsky, A., A. Aikio, T. Turunen, H. Nilsson, T. Sergienko, V. Safargaleev, and K. Kauristie (2007), Dynamics and electric currents of morningside Sun-aligned auroral arcs, *J. Geophys. Res.*, **112**, A06306, doi:10.1029/2006JA012244.
- Lu, J. Y., W. Wang, R. Rankin, R. Marchand, J. Lei, S. C. Solomon, I. J. Rae, J.-S. Wang, and G.-M. Le (2008), Electromagnetic waves generated by ionospheric feedback instability, *J. Geophys. Res.*, **113**, A05206, doi:10.1029/2007JA012659.
- Lysak, R. L. (1986), Coupling of the dynamic ionosphere to auroral flux tube, *J. Geophys. Res.*, **91**(A6), 7047–7056.
- Lysak, R. L. (1988), Theory of auroral zone PiB pulsation spectra, *J. Geophys. Res.*, **93**(A6), 5942–5946, doi:10.1029/JA093iA06p05942.
- Lysak, R. L. (1991), Feedback instability of the ionospheric resonant cavity, *J. Geophys. Res.*, **96**(A2), 1553–1568, doi:10.1029/90JA02154.
- Lysak, R. L., and Y. Song (2002), Energetics of the ionospheric feedback interaction, *J. Geophys. Res.*, **107**(A8), 1160, doi:10.1029/2001JA000308.
- Miura, A., and T. Sato (1980), Numerical simulation of global formation of auroral arcs, *J. Geophys. Res.*, **85**(A1), 73–91, doi:10.1029/JA085iA01p00073.
- Newell, P. T., C.-I. Meng, and K. M. Lyons (1996), Suppression of discrete aurora by sunlight, *Nature*, **381**, 766–767.
- Newell, P. T., C.-I. Meng, and S. Wing (1998), Relation of solar activity of intense aurorae in sunlight and darkness, *Nature*, **393**, 342–344.
- Nilsson, H., A. Kozlovsky, T. Sergienko, and A. Kotikov (2005), Radar observations in the vicinity of pre-noon auroral arcs, *Ann. Geophys.*, **23**, 1785–1796.
- Ogawa, T., and T. Sato (1971), New mechanism of auroral arcs, *Planet. Space Sci.*, **19**(11), 1393–1412.
- Park, R. J., and P. A. Cloutier (1971), Rocket-based measurements of Birkeland currents related to an auroral arc and electrojet, *J. Geophys. Res.*, **76**(31), 7714–7733.
- Pokhotelov, D., W. Lotko, and A. V. Streltsov (2002a), Effects of the seasonal asymmetry in ionospheric Pedersen conductance on the appearance of discrete aurora, *Geophys. Res. Lett.*, **29**(10), 1437, doi:10.1029/2001GL014010.
- Pokhotelov, D., W. Lotko, and A. V. Streltsov (2002b), Harmonic structure of field line eigenmodes generated by ionospheric feedback instability, *J. Geophys. Res.*, **107**(A11), 1363, doi:10.1029/2001JA000134.
- Robinson, R. M., E. A. Bering, R. R. Vondrak, H. R. Anderson, and P. A. Cloutier (1981), Simultaneous rocket and radar measurements of currents in an auroral arc, *J. Geophys. Res.*, **86**(A9), 7703–7717.
- Sato, T. (1978), A Theory of quiet auroral arcs, *J. Geophys. Res.*, **83**(A3), 1042–1048.
- Sato, T. (2005), Macro-micro interlocked simulator, *J. Phys. Conf. Ser.*, **16**, 310–316, doi:10.1088/1742-6596/16/1/043.
- Sato, T., and T. E. Holzer (1973), Quiet auroral arcs and electrodynamic coupling between the ionosphere and the magnetosphere, 1, *J. Geophys. Res.*, **78**(31), 7314–7329.
- Sato, T., and T. Iijima (1979), Primary sources of large-scale Birkeland currents, *Space Sci. Rev.*, **24**(3), 347–366.
- Sato, T., and H. Okuda (1980), Ion-acoustic double layers, *Phys. Rev. Lett.*, **44**(11), 740–743.
- Sato, T., H. Hasegawa, and N. Ohno (2009), Macro-micro interlocked simulation algorithm: An exemplification for aurora arc evolution, *Comput. Sci. Discovery*, **2**, 015007, doi:10.1088/1749-4699/2/1/015007.
- Streltsov, A. V., and W. Lotko (2003), Small-scale electric fields in downward auroral current channels, *J. Geophys. Res.*, **108**(A7), 1289, doi:10.1029/2002JA009806.
- Streltsov, A. V., and W. Lotko (2004), Multiscale electrodynamics of the ionosphere-magnetosphere system, *J. Geophys. Res.*, **109**, A09214, doi:10.1029/2004JA010457.

- Trakhtengertz, V. Y., and A. Y. Feldstein (1984), Quiet auroral arcs: Ionospheric effect of magnetospheric convection stratification, *Planet. Space Sci.*, 32(2), 127–134.
- Watanabe, K., and T. Sato (1988), Self-excitation of auroral arcs in a three-dimensionally coupled magnetosphere-ionosphere system, *Geophys. Res. Lett.*, 15(7), 717–720.
- Watanabe, K., and T. Sato (1990), Global simulation of the solar wind-magnetosphere interaction: The importance of its numerical validity, *J. Geophys. Res.*, 95(A1), 75–88.
- Watanabe, K., M. Ashour-Abdalla, and T. Sato (1986), A numerical model of the magnetosphere-ionosphere coupling: Preliminary results, *J. Geophys. Res.*, 91(A6), 6973–6978.
- Watanabe, T.-H., H. Oya, K. Watanabe, and T. Sato (1993), Comprehensive simulation study on local and global development of auroral arcs and field-aligned potentials, *J. Geophys. Res.*, 98(A12), 21,391–21,407.
- 
- H. Hasegawa, Department of Helical Plasma Research, National Institute for Fusion Science, 322-6 Oroshi-cho, Toki, Gifu 509-5292, Japan.
- N. Ohno, Earth Simulator Center, Japan Agency for Marine-Earth Science and Technology, 3173-25 Showa-machi, Kanazawa-ku, Yokohama, Kanagawa 236-0001, Japan.
- T. Sato, University of Hyogo, 1-3-3 Higashikawasaki-cho, Chuo-ku, Kobe, Hyogo 650-0044, Japan.